Journal of Metals, Materials and Minerals, 37(2), e2774, 2027

Influence of solution nitriding and annealing on the abrasive wear behavior of 201J1 austenitic stainless steel

Witchaya CHUEACHANPOL[1], Nithi SAENARJHAN[1], and Jatupon OPAPAIBOON[1,*]

[1] *Department of Metallurgical Engineering, Faculty of Engineering, Chulalongkorn University, Phayathai Road, Bangkok, 10330, Thailand*

***Corresponding author e-mail**: Jatupon.O@chula.ac.th,

Received date:
9 June 2026
Revised date:
21 July 2026
Accepted date:
29 September 2026

Keywords:
Austenitic stainless steel;
Solution nitriding;
Abrasive wear;
Strain-induce transformation

Abstract

This study investigates the effects of high-temperature solution nitriding (SLN) and subsequent annealing (SLN+AN) on the microstructural and tribological properties of 201J1 austenitic stainless steel. Specimens were nitrided at 1050°C and annealed at 1200°C, followed by reciprocating sliding wear tests under applied loads of 10 N, 30 N, and 50 N. Results showed that the SLN+AN treatment successfully formed a highly hardened surface layer (~ 25 µm, 587.2 HV) over a ductile austenite matrix, establishing a clear hardness gradient. Tribological testing demonstrated a distinct load-dependent wear behavior. Under low to moderate loads (10 N to 30 N), the SLN+AN specimen exhibited superior wear resistance and significantly shallower wear depths compared to the as-received (AR) and SLN conditions. However, at a high load of 50 N, the SLN+AN specimen transitioned to severe wear, recording the highest mass loss (2.6 mg) due to the brittle fracture of the surface-modified layer. Furthermore, nanoindentation confirmed that sliding induced surface strain hardening. While this transformation lowered the coefficient of friction at high loads, its inherent brittleness accelerated material loss. These results show that while SLN+AN effectively enhances surface hardness, balancing hardness and ductility is key for ensuring wear resistance in severe tribological applications.

1. Introduction

Austenitic stainless steels are widely acknowledged as the most widely used group of stainless steels, accounting for approximately 70% of total use. Their primary microstructural constituent is austenite (γ-phase), which possesses a face-centered cubic (FCC) crystal structure. This structure imparts excellent corrosion resistance, ductility, and formability, enabling their widespread use in industrial components, agricultural machinery, biomedical devices, and household appliances [1,2]. However, austenite is metastable and can undergo strain-induced phase transformations under mechanical loading, typically following the sequence γ (austenite) → ε (hexagonal close-packed martensite) → α′ (body-centered tetragonal martensite), also referred to as strain-induced martensite [1,3,4]. These transformations increase strength but also make the material brittle, potentially affecting its wear resistance and practical applications.

In recent years, efforts have been made to reduce the nickel content in austenitic stainless steels, replacing it with higher levels of manganese and nitrogen, which act as austenite stabilizers, primarily due to cost considerations. This development has led to the introduction of 200-series austenitic stainless steels. [4–8] However, both 200-series and 300-series steels exhibit relatively poor tribological and limited mechanical properties, making them susceptible to damage and wear under mechanical or abrasive conditions. One of the most commonly observed wear mechanisms is abrasive wear, which occurs through contact between two surfaces, where the lower-wear-resistance surface experiences more severe material loss [9–11]. In certain applications, such as biomedical devices, materials are required to exhibit both high wear resistance and excellent corrosion resistance [11]. While the reduced nickel content in 200-series steels offers advantages in cost and biocompatibility [12], their wear resistance remains limited.

To overcome the limited wear resistance of austenitic stainless steels, high-temperature gas nitriding has been employed as a surface treatment. During this process, nitrogen diffuses into the steel surface at elevated temperatures, forming expanded austenite (γ′) or nitride-enriched layers. These surface layers increase hardness and enhance resistance to abrasive wear while maintaining inherent corrosion resistance [13–15]. While high-temperature nitriding and post-nitriding annealing are well-documented for conventional 300-series stainless steels, the 201J1 grade is well-known and widely used in the stainless steel market, requiring a dedicated investigation. Because it substitutes costly nickel (Ni) with manganese (Mn) and nitrogen (N), its phase stability at high temperatures changes significantly, meaning the mechanisms from 300-series steels cannot be directly applied.

In this study, 201J1 austenitic stainless steel was selected as the base material. High-temperature gas nitriding (SLN) at 1050°C, followed by annealing (AN) at 1200°C, was applied to modify the specimens. Since precipitates dissolve above 1150°C, an annealing temperature of 1200°C was chosen to maximize the nitrogen solid solution at the surface while ensuring the complete dissolution of any carbides or nitrides formed during the nitriding process. Furthermore, while most existing literature on surface-treated austenitic stainless steels focuses heavily on corrosion, the tribological behavior of this specific industrial grade remains rarely explored. This study provides new empirical

evidence on how SLN and SLN+AN treatments influence the wear behavior of 201J1, demonstrating how this cost-effective alloy can be upgraded for applications requiring higher wear resistance.

2. Experimental details

2.1 Material and specimen preparation

Austenitic stainless steel grade 201J1 was selected as the experimental material in this study. Its chemical composition, determined by Spark Optical Emission Spectrometer (Spark-OES, BRUKER Q8 Magellan), is presented in Table 1. The material was received as cold-rolled plates with a thickness of 1.2 mm.

The specimens were subjected to solution nitriding at 1050°C for 1 h under an N_2 atmosphere at 80 kPa, following the heating profile shown in Figure 1. After nitriding, half of the specimens were subsequently annealed at 1200°C for 1 h under a vacuum atmosphere of 1 Torr (133 Pa) and cooled with nitrogen gas down to 50°C, following the heating profile presented in Figure 2, to evaluate the influence of post-treatment thermal processing. Based on these treatments, the specimens were classified into three conditions: 1) As-received (AR), 2) Solution nitriding (SLN), 3) Solution nitriding followed by annealing (SLN+AN)

The specimens were initially sectioned using a cutting machine (Labotom-5) for size reduction, and subsequently cut to final dimensions of 3.5 cm × 2 cm × 1.2 mm (length × width × thickness) using a precision cutting machine (Accutom-5) to ensure high dimensional accuracy and uniformity. The samples were subsequently ground sequentially using abrasive papers with grit sizes ranging from 80 to 2000, followed by fine polishing with 1 µm diamond paste. Specimens from all three conditions were randomly selected, with eight samples per condition used for surface roughness measurements to determine the average Ra value. Surface roughness was not strictly controlled in this experiment better simulate the actual service conditions of the specimens.

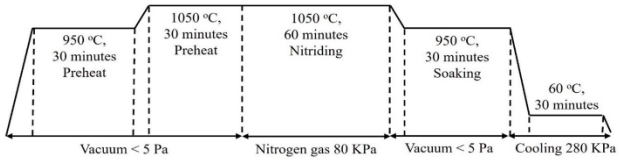

Figure 1. Condition of the Solution nitriding process on 201 J1.

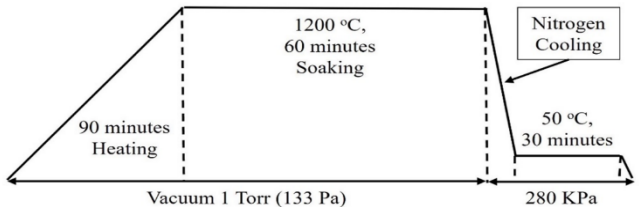

Figure 2. Condition of the annealing process after the solution nitride gas treatment on 201 J1.

Table 1. Chemical composition of 201 J1.

Alloy element	C	Cr	Cu	Si	P	S	Mn	Ni	N	Fe
Mass %	0.095	13.82	1.18	0.42	0.039	0.005	9.98	1.03	0.146	Bal.

The etching process was carried out using an electro-etching technique with 10% oxalic acid at 7 V for 30 s. After etching, the microstructural characteristics were examined using an optical microscope (OM, Zeiss Axio Lab.A1). Observations focused on cross-sectional areas evaluate microstructural evolution induced by different heat treatment conditions.

2.2 Hardness measurement

Microhardness measurements were performed using a Vickers microhardness tester (HM-200, Mitutoyo) with an applied load of 0.05 kg. For hardness evaluation along the longitudinal direction, indentations were made at the central region of each specimen, and the average value was reported as the representative hardness. For cross-sectional hardness measurements, measurement points were taken from one edge of the specimen to the opposite edge to determine the hardness distribution from surface to surface in the surface-treated specimens. A spacing of 100 µm was used between measurement points, while a closer spacing of 10 µm was applied in the near-surface region where higher hardness values were observed. The resulting hardness depth profile was reported as the cross-sectional hardness distribution. For the SLN specimen, hardness measurements near the surface were obtained in the same manner as for the SLN+AN specimen. In the SLN+AN specimen, hardness values were obtained from the surface-modified layer and the bulk region.

After tribological testing, the specimens were sectioned along a cross-section through the center of the wear track using a precision cutting machine (Accutom-5). Nanoindentation tests were then performed to evaluate the subsurface hardness beneath the wear tracks generated at tribological loads of 10 N and 30 N. The tests were conducted using a Micro-hardness tester (PICODENTOR® HM500, Fischer) with a suitably sized indentation array to fully cover the subsurface region beneath the wear track. The results were mapped as hardness values across the x-y plane, from the top-left to the bottom-right of the target area. The tests were conducted with an applied load of 200 mN, a loading time of 20 s, a holding (creep) time of 5 s, and unloading under the same conditions. These measurements were carried out to evaluate hardness variations and to correlate them with the microstructural modifications induced by the applied loads during tribological testing.

2.3 Tribological test and characterization

Dry sliding wear tests were conducted using a tribometer (Ducom Unitest: Universal Tribotester) under reciprocating sliding conditions. The test methods and procedures were adapted from the ASTM G133-05 standard [16], and the tests were performed under applied loads of 10 N, 30 N, and 50 N. The tests were performed at a speed of 30 $mm \cdot s^{-1}$, with a stroke length of 1 cm and a total test duration of 15 min, over the same area from start to stop. Test specimens were used, and an alumina ball with a diameter of 6.35 mm served as the counterbody

During testing, the coefficient of friction (COF) was continuously recorded to monitor frictional behavior under different loading conditions. Wear loss was determined using a four-digit analytical balance with limited resolution of 0.1 mg (0.0001 g). by measuring the mass before and after the 15 min sliding test. Each wear test was repeated three times to obtain the average values. Prior to each weighing procedure, the specimens were ultrasonically cleaned in absolute ethanol. All wear tests were carried out under ambient laboratory conditions.

The worn surfaces of the specimens were examined using confocal laser scanning microscopy (CLSM, Olympus LEXT OLS5000). CLSM scans at 100X magnification were used to obtain two-dimensional wear track profiles and measurement of wear depth. These profiles were analyzed to evaluate the wear resistance of surface-treated specimens relative to untreated specimens, thereby highlighting differences in wear behavior resulting from the applied surface treatments under different tribological loading conditions. The worn surfaces were also investigated using a scanning electron microscope (SEM, JEOL JSM-IT300) at an accelerating voltage of 15 kV and at various magnifications. Images were captured to cover both the center and the edges of the wear tracks for all specimens to determine the wear mechanisms observed during the highest applied load test.

3. Results and discussion

3.1 Microstructure of test specimens

The microstructures of the test specimens under different heat treatment conditions are shown in Figure 3. The AR specimen exhibited a fine austenite (γ) grain structure, as shown in Figure 3(a), which is consistent with its processing history, since the base material was received in the cold-rolled condition with an average grain size of approximately 10 µm.

In contrast, the SLN specimen exhibited significant microstructural evolution. Following electro-etching, optical microscopy (OM) revealed a distinctly darker near-surface region compared to the relatively uniform, coarse austenite (γ) grains (approximately 75 µm to 100 µm) in the central region (Figure 3(b)). This central grain coarsening resulted from the elevated processing temperatures. Meanwhile, the darker appearance near the surface is attributed to carbide or nitride precipitation along the boundaries of the finer grains (approximately 25 µm to 50 µm) formed during nitriding. These precipitates induce localized chromium depletion and affect sensitization, which reduces corrosion resistance and causes these specific regions to be preferentially attacked by the etchant.[1,14,17,18].

For the SLN+AN specimen, a distinct surface-modified layer with a thickness of approximately 25 µm was observed near the treated surface. The austenite (γ) grain size in the bulk region further increased to values exceeding 100 µm, as shown in Figure 3(c). This grain growth is attributed to the annealing treatment at 1200°C for 1 h, as illustrated in Figure 2. [19,20] The annealing treatment promoted grain coarsening in the bulk region, while the surface-modified layer appeared, resulting in a microstructure with a modified surface layer over a coarse austenite matrix.

3.2 Influence of solution nitriding and annealing processes on micro-vickers hardness and surface roughness profiles

According to Figure 3, the AR specimen exhibited a fine austenite grain structure resulting from cold rolling. Micro-vickers hardness measurements revealed an average hardness of 287.09 HV. For the SLN specimen, grain coarsening of the austenite structure was observed, resulting in a decrease in the average hardness in the central region to 238.65 HV. In contrast, the near-surface region exhibited a slightly higher hardness of 258.71 HV, as shown in Table 2. This increase in near-surface hardness can be attributed to carbide precipitation along grain boundaries, which provides greater hardness than the coarse-grained bulk region. [21]

In the SLN+AN specimen, the average hardness in the coarse-grained bulk region was 241.63 HV, which is comparable to that of the SLN specimen. A substantial increase in hardness was observed in the outer layer, where the average hardness reached 587.2 HV (Table 2). The intermediate region between the outer layer and the core material exhibited an intermediate hardness of 409.98 HV. Hardness measurements along the cross-sectional direction revealed that the SLN+AN specimen exhibited the highest hardness at the surface, followed by a gradual decrease toward the center of the specimen, before increasing again to reach a maximum at the opposite surface., as shown in Figure 4. This high surface hardness is expected to significantly enhance the wear resistance of the SLN+AN specimen by providing a hard surface while retaining a comparatively softer and tougher core material [15,20,22–24], as further evaluated through tribological testing.

In addition to microstructural and hardness modifications, the surface treatments significantly influenced the surface topography. Surface roughness measurements showed that the average roughness (Ra) increased from 0.1353 µm in the AR specimen to 0.2059 µm in the SLN specimen, and further to 0.2910 µm in the SLN+AN specimen. These results indicate that both surface treatment processes led to a progressive increase in surface roughness compared with the AR condition. Among the three conditions, the SLN+AN specimen exhibited the highest surface roughness, indicating that the combined effects of nitriding and annealing produced a more significant modification of the surface morphology.

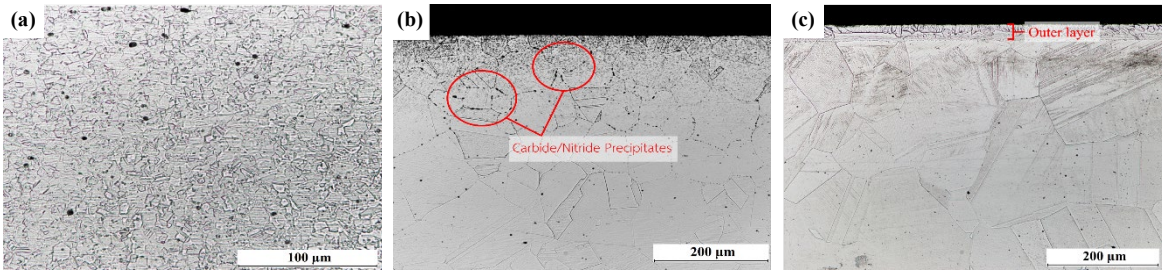

Figure 3. Microstructures of the specimens: (a) As-received (AR) at 500X magnification, (b) SLN at 200X magnification, and (c) SLN+AN at 200X magnification.

Table 2. Average Micro-Vickers hardness of As-received (AR), Solution nitriding (SLN), Solution nitriding followed by annealing (SLN+AN) specimens.

Condition	Location	Average hardness (HV 0.05 kg.f.)	SD
AR	-	287.09	24.47
SLN	Core	238.65	15.17
	Side	258.71	15.86
SLN+AN	Outer layer	587.2	51.35
	Core	241.63	26.28

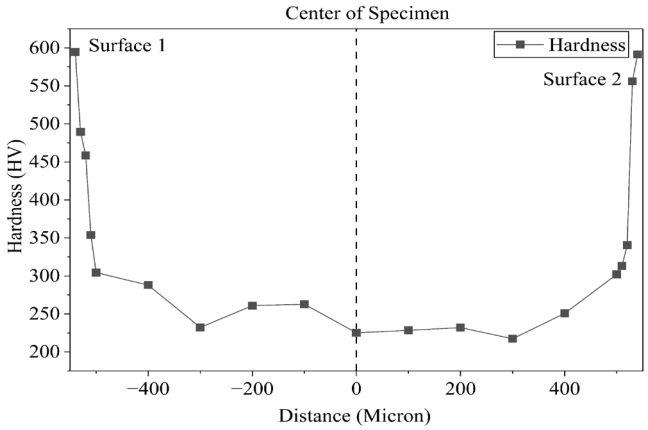

Figure 4. Cross-section hardness of SLN+AN specimen.

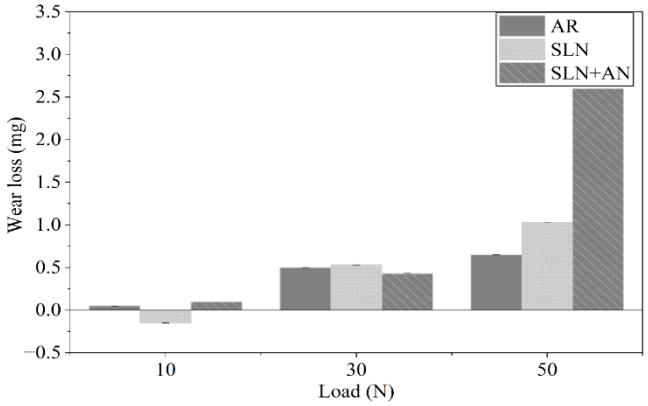

Figure 5. Wear loss for each specimen compared to an applied load.

Consequently, the tribological behavior of the treated specimens will be governed by surface properties. While the high surface hardness of the SLN+AN specimen is expected to improve wear resistance, the increased surface roughness is an important factor that may heavily influence the frictional response, particularly the coefficient of friction (COF), as further evaluated through the following tribological tests [9,11,25].

3.3 Tribological testing

3.3.1 Influence of solution nitriding and annealing processes on wear loss

As shown in Figure 5, under an applied load of 10 N for 15 min of sliding, the AR specimen showed a minor mass loss of approximately 0.1 mg, indicating no significant material removal. Similarly, the SLN specimen recorded a negative mass loss of approximately –0.1 mg, indicating a slight mass increase. This minor weight gain can be attributed to the transfer and accumulation of wear debris from the alumina counterbody onto the wear track. The SLN+AN specimen also exhibited a minimal mass loss of merely 0.1 mg. Overall, these results indicate that the low applied load of 10 N while machine limitation was indicate with 0.1 mg the small amount of mass change could be identified as insufficient to cause significant material removal in any of the specimens, despite their differences in surface conditions and microstructural characteristics.

When the applied load was increased to 30 N, a noticeable increase in wear loss was observed for all specimens. The AR specimen exhibited an average wear loss of 0.50 mg, while the SLN specimen showed a slightly higher average wear loss of 0.53 mg. The SLN+AN specimen maintained the highest wear resistance with a minimal wear loss of 0.43 mg due to its highest surface hardness. Overall, the wear losses at 30 N were significantly higher than those at 10 N, indicating that increasing the applied load enhanced material removal during sliding.

At the highest applied load of 50 N, the wear loss of all specimens increased markedly, consistent with the general trend that higher loads promote more severe wear. [9,21,26–29] The AR specimen exhibited an average wear loss of 0.65 mg, whereas the SLN specimen showed a higher wear loss of 1.0 mg. In contrast, the SLN+AN specimen exhibited a substantially greater wear loss, averaging 2.6 mg. Despite its high surface hardness, the SLN+AN specimen exhibited the lowest wear resistance under a 50 N load. This behavior suggests that, under high-load conditions, the hard but brittle surface-modified layer in the SLN+AN specimen accelerated material removal compared to the other specimens, which retained more ductile austenite microstructures [23,30,31].

3.3.2 Analysis of the worn surface

Confocal laser scanning microscopy (CLSM) was employed to examine the morphology of the wear track under different applied loads and to correlate the observed wear features with the resulting wear loss. In addition to surface morphology, CLSM generated 3D topographical images to quantify the depth of the wear tracks. Cross-sectional profiles were extracted from the central regions of the wear tracks to evaluate the maximum wear depth under each testing condition.

Wear depths were measured at the center of the wear tracks, as illustrated in Figure 6(a–c). At an applied load of 10 N, the central wear regions were relatively shallow, as shown in Figure 6(a). Specifically, the AR and SLN specimens showed comparable central wear depths of 9.802 μm and 9.721 μm, respectively, whereas the SLN+AN specimen exhibited a significantly shallower wear depth of 4.241 μm. The shallow wear track observed in the SLN+AN specimen is consistent with the negligible wear loss measured under a 10 N load and reflects the specimen's high surface hardness, which effectively resisted material removal under low-load sliding conditions [15, 21, 32].

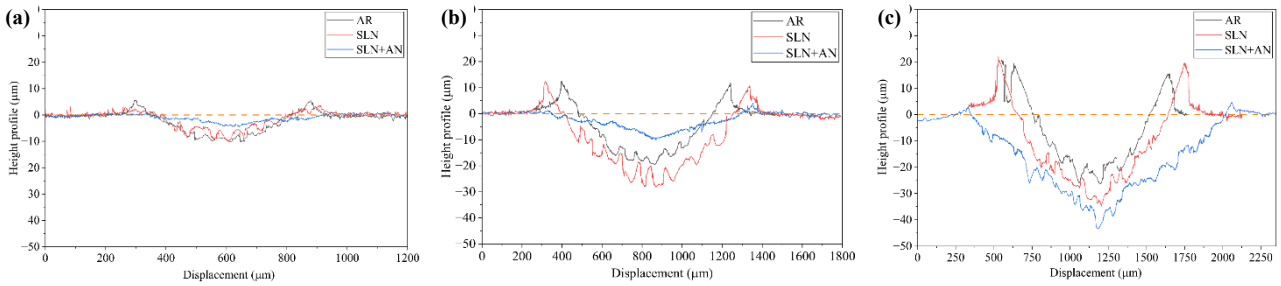

Figure 6. Wear depths measured at the central region of the wear tracks for each specimen under applied loads of (a) 10 N, (b) 30 N, and (c) 50 N.

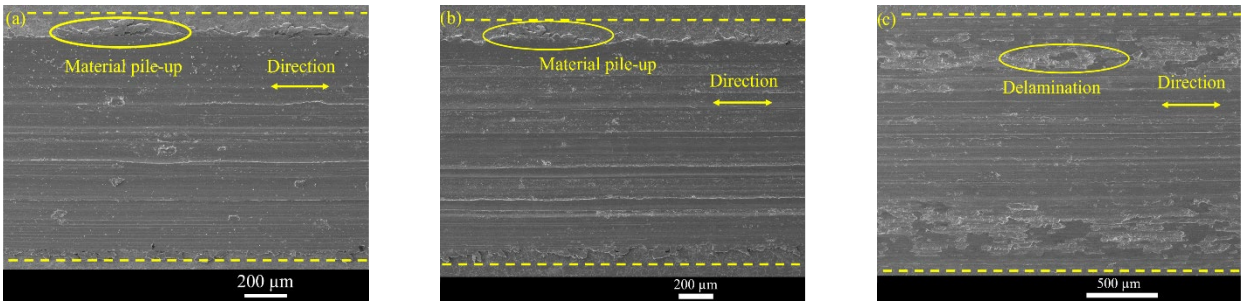

Figure 7. SEM micrographs of wear track under load 50 N (a) AR at 75X magnification, (b) SLN at 60X magnification, and (c) SLN+AN at 50X magnification.

As shown in Figure 6(b), when the applied load was increased to 30 N, the wear depths of the AR and SLN specimens increased markedly to 18.129 μm and 28.061 μm, respectively. In contrast, the SLN+AN specimen maintained a relatively low wear depth of 9.815 μm. Although the wear depths differed among the specimens, the overall wear losses remained comparable, ranging from approximately 0.45 mg to 0.50 mg. This behavior can be attributed to the high ductility of the austenite microstructure in the AR and SLN specimens, which promoted plastic deformation and material pile-up at the wear track edges rather than direct material removal [17,30,31]. This pile-up, evident in the wear tracks (Figure 6(a–c)), contributed to a reduction in the effective wear loss despite the increased groove depth. Meanwhile, the hard surface-modified layer in the SLN+AN specimen limited plastic deformation, resulting in a shallower wear track and more stable wear behavior under this intermediate load.

At the highest applied load of 50 N (Figure 6(c)), the AR and SLN specimens exhibited comparable wear depths of 26.133 μm and 30.763 μm, respectively, together with moderate increases in wear loss (0.65 mg for the AR specimen and 1.0 mg for the SLN specimen). This response is consistent with their austenite microstructures, which retained sufficient ductility to accommodate plastic deformation and promote material pile-up along the wear track edges, which minimized the increase in wear loss for the AR and SLN specimens (Figure 5), thereby limiting excessive material removal despite the increased load., thereby limiting excessive material removal despite the increased load. Conversely, the SLN+AN specimen exhibited a drastic increase in wear depth to 43.478 μm and the highest wear loss of 2.6 mg, despite possessing the highest surface hardness. CLSM observations revealed a significantly wider wear track and markedly reduced material pile-up at the groove edges compared with the AR and SLN specimens, as shown in Figure 6(c). This behavior indicates that, once the hard surface-modified layer fractured under the high applied load, the wear mechanism transitioned from mild to severe wear, as shown in Figure 5 [23,30,31]. Consequently, the initially beneficial high hardness of the SLN+AN specimen no longer contributed to improved wear resistance under severe loading conditions. To further investigate the factors governing this wear behavior, the initial surface roughness and the coefficient of friction (COF) were evaluated.

To observe the wear mechanisms contributing to mass loss under the 50 N load which is the highest load in this study, SEM micrographs of the wear tracks were analyzed, as shown in Figure 7(a–c). As seen in Figure 7(a), the AR specimen clearly shows a reciprocating sliding direction from left to right on the same area. As shown in Figure 6(c), the CLSM results indicate that the AR specimen exhibits material pile-up at the wear track edges, as indicated by the yellow circles. Similarly, the SLN specimen (Figure 7(b)) exhibited the same tribological behavior as the AR specimen, showing material pile-up and a clear sliding direction. However, for the SLN+AN specimen (Figure 7(c)), although the sliding direction was clearly visible, no material pile-up was observed at the wear track edges. Instead, it revealed a delamination mechanism, indicating brittle surface fracture. This brittle fracture led to a significant increase in wear loss and wear depth under the 50 N load, as previously shown in Figure 5 and Figure 6(c). Overall, an examination of all worn surfaces in Figure 7 confirms that abrasive wear occurred across all specimens. This is evidenced by the distinct parallel grooves aligned with the sliding direction, a characteristic feature of a two-body abrasive wear mechanism [9].

3.3.3 Coefficient of friction

The average coefficient of friction (COF) values under varying applied loads are presented in Figure 8. At an applied load of 10 N, the AR, SLN, and SLN+AN specimens exhibited average COF values of 0.383, 0.777, and 0.969, respectively. This progressive increase in COF from the AR to the SLN+AN condition was consistently observed across all tested loads. At 30 N, the COF values were 0.405 (AR), 0.538 (SLN), and 0.792 (SLN+AN), while at 50 N, they were 0.399, 0.448, and 0.571, respectively.

The observed trend at the initial 10 N load correlates directly with the initial surface roughness (Ra) of the specimens, as reported in Section 3.2. Surface roughness is a critical parameter influencing frictional behavior, as higher Ra values promote mechanical interlocking and enhance asperity interactions at the contact interface, thereby increasing the COF [9,11]. Consequently, the SLN+AN specimen, which possessed the highest surface roughness, consistently exhibited the highest friction.

Furthermore, a clear load-dependent frictional behavior was evident for the treated specimens. The SLN and SLN+AN specimens recorded their highest COF values at the lowest load (10 N), followed by a gradual decrease as the load increased to 30 N and 50 N. This behavior is associated with the high surface hardness and near-surface precipitation in the modified layers. At elevated loads, changes in the real contact area significantly affect the frictional behavior, leading to a reduction in the COF [15]. In contrast, the AR specimen maintained a relatively stable COF (approximately 0.38 to 0.40) across applied loads, as shown in Figure 8. This stability can be attributed to the early onset of strain hardening, which appears to occur even under the relatively low load of 10 N.

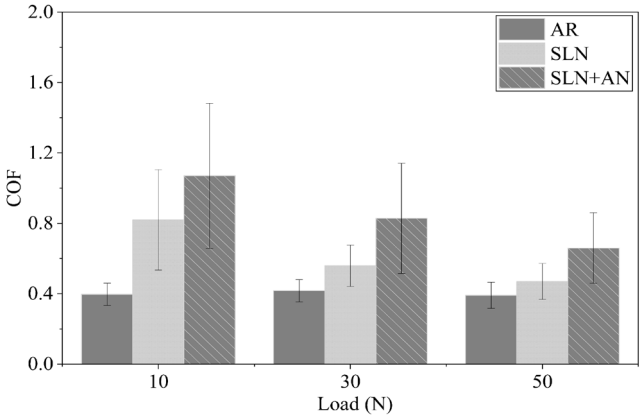

Figure 8. Average coefficient of friction for each specimen as a function of applied load.

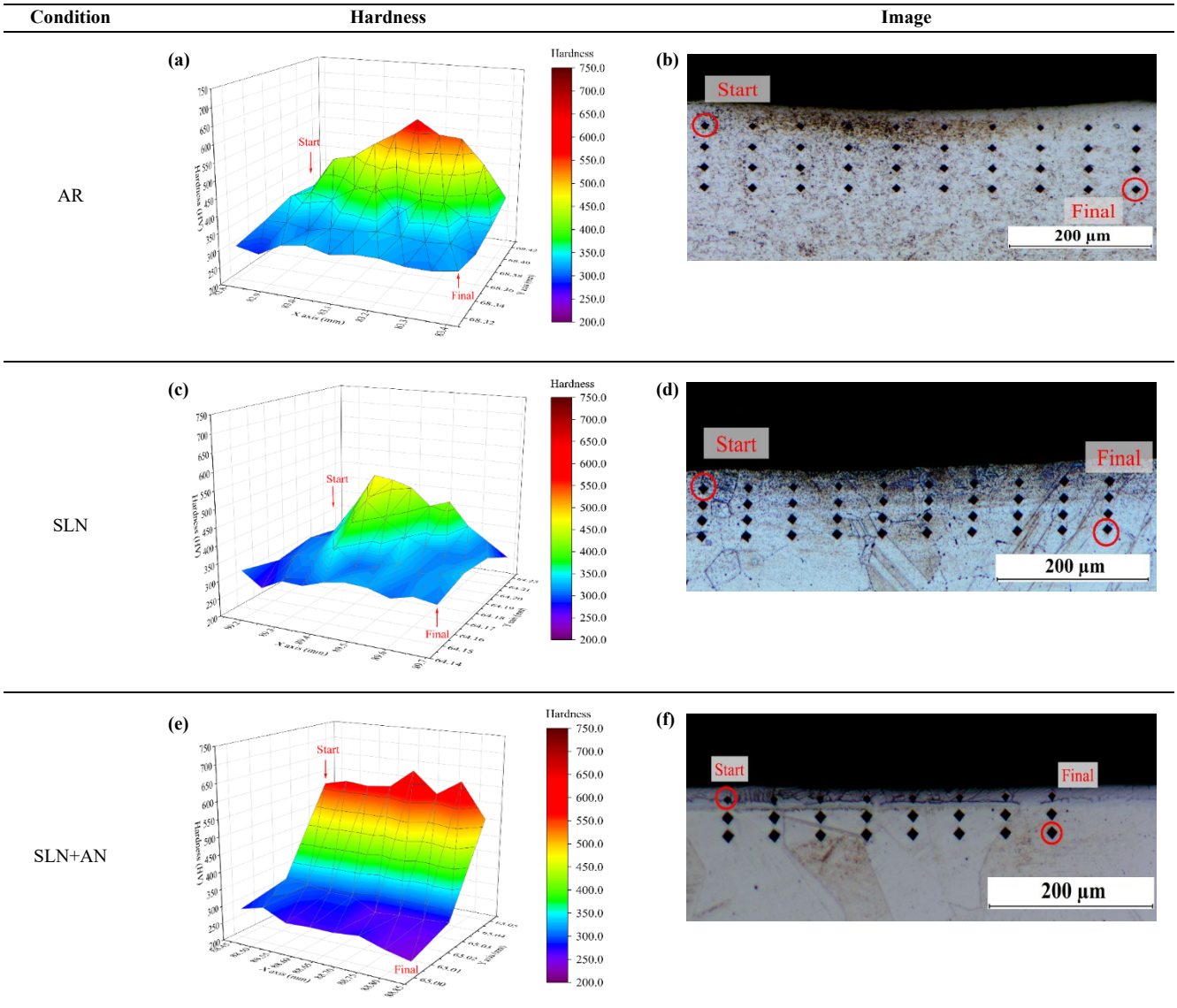

Figure 9. Hardness 3D profile and nanoindentation image under 200 X magnification under 10 N load (a) Hardness (AR), (b) Image (AR), (c) Hardness (SLN), (d) Image (SLN), (e) Hardness (SLN+AN), and (f) Image (SLN+AN).

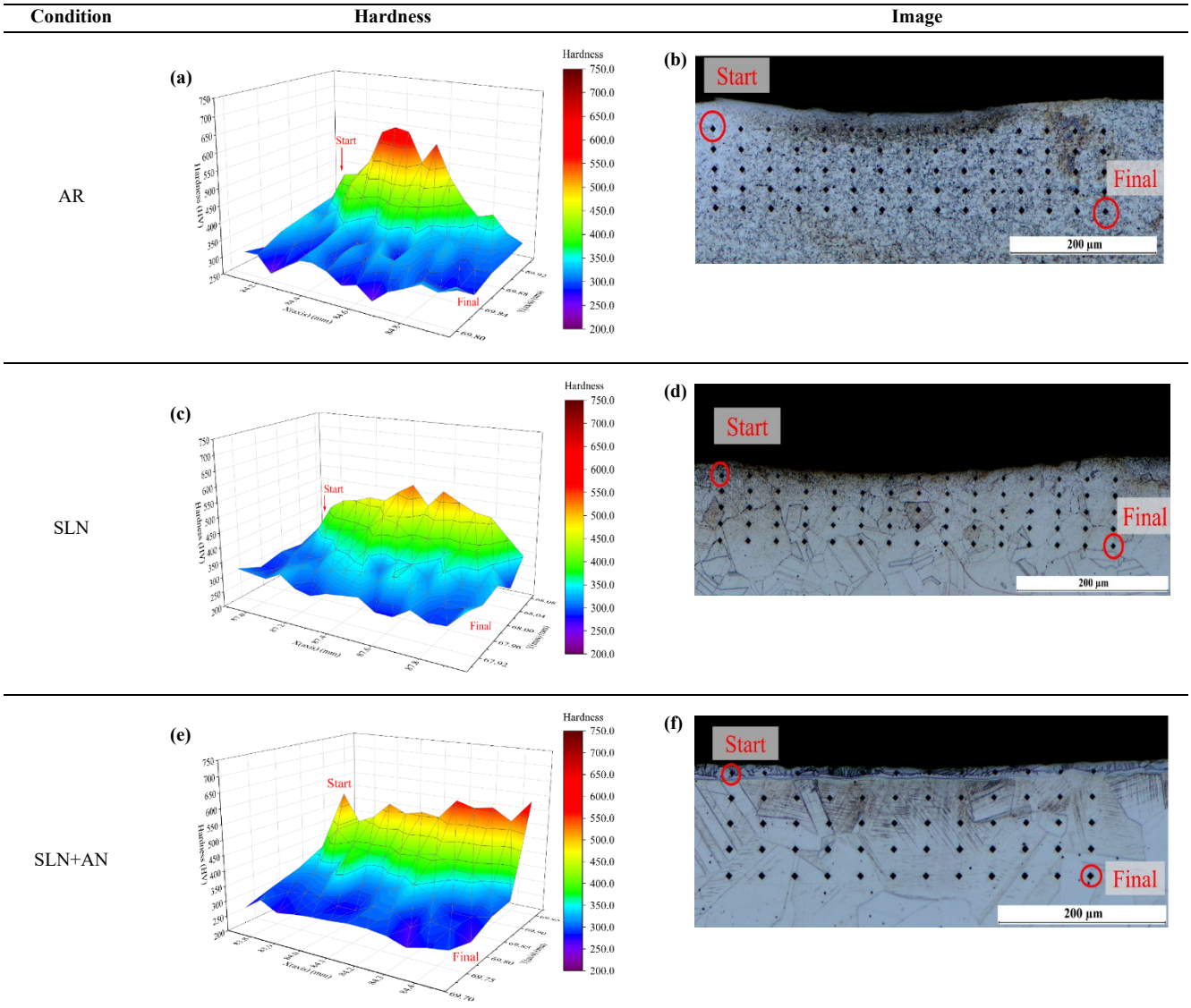

Figure 10. Hardness 3D profile and nanoindentation image under 200 X magnification under 30 N load (a) Hardness (AR), (b) Image (AR), (c) Hardness (SLN), (d) Image (SLN), (e) Hardness (SLN+AN), and (f) Image (SLN+AN).

Overall, these results indicate that the frictional response is governed by the combined effects of initial surface conditions and applied load. Although the rougher-treated specimens initially exhibited higher friction, their COF values decreased under heavier loads. This reduction correlates with the surface strain hardening of the wear tracks [33,34], as revealed by the following nanoindentation analysis. These findings highlight the important role of surface conditions in controlling frictional response during reciprocating sliding.

3.3.4 Nanoindentation

At an applied load of 10 N (Figure 9(a–f)), The measurements were mapped into hardness values across the x-y position, from the top-left to the bottom-right of the provided micrographs. The AR and SLN specimens exhibited a marked increase in hardness beneath the wear tracks, with maximum hardness values of approximately 550 HV and 450 HV, respectively. These values are significantly higher than the original hardness of the austenite microstructure measured before tribological testing, indicating that the low stability of the austenite microstructure led to surface strain hardening. In contrast, the SLN+AN specimen showed no significant change in hardness beneath the wear track, suggesting that the Applied load was insufficient to damage or plastically deform the hard surface-modified layer. Consequently, the measured hardness reflects the surface layer's initial hardness.

When the load was increased to 30 N (Figure 10(a–f)), further hardening beneath the wear tracks was observed across all specimens. The AR specimen exhibited subsurface hardness values exceeding 600 HV, while the SLN specimen reached over 550 HV. For the SLN+AN specimen, partial degradation of the surface-modified layer exposed of the underlying austenite matrix, resulting in a substantial increase in subsurface hardness to approximately 500 HV. This overall surface hardening is attributed to strain-induced transformations, including the formation of mechanical twins and martensite, which are clearly visible in Figure 16 (b) [30,33–37].

These results demonstrate that tribological sliding induces significant strain hardening in the austenite microstructure. It can be assumed

that this behavior would still occur under a higher load (50 N). This hardening is result of severe work hardening or strain hardening beneath the wear track. These various deformation mechanisms are inherent to metastable austenitic stainless steels, including dislocation interaction, mechanical twinning, and potentially strain-induced martensitic transformation ($\gamma \rightarrow \varepsilon \rightarrow \alpha'$), which typically occurs under severe plastic deformation [30,33,35,37]. This microstructural transformation correlates directly with the frictional behavior observed in this study (Figure 8). For instance, the stable COF of the AR specimen across different loads can be explained by the fact that work hardening had already affected near the worn surface even under the lowest load of 10 N. This trend is also evident in the surface-treated specimens, where a significant decrease in COF was observed as the applied load increased.

However, analysis of wear loss as a function of applied load reveals that the increased hardness does not correspond to improved in wear resistance. In both the AR and SLN specimens, wear loss continued to increase steadily with the applied load, despite the pronounced surface hardening. At the highest applied load of 50 N, the SLN+AN specimen exhibited a drastic increase in wear loss (Figure 5 and Figure 6(c)) despite its high hardness. This indicates that while the strain-induced martensite provides high hardness, it is inherently brittle. Furthermore, the SLN+AN specimen exhibited lower overall ductility than the other specimens, as evidenced by significantly reduced material pile-up at the wear track edges. Consequently, once the hard surface-modified layer and the transformed surface region fractured under high stress, rapid material removal occurred [21,23].

This explanation is further supported by wear depth measurements. The AR specimen exhibited a nearly linear increase in wear depth with increasing load, while the SLN specimen showed only a slight increase from 30 N to 50 N, reflecting the ductile deformation behavior. In contrast, the rapid increase in wear depth for the SLN+AN specimen at 50 N indicates a transition to a brittle-dominated wear mechanism under severe loading conditions.

4. Conclusions

This study investigated the effects of high-temperature solution nitriding (SLN) and subsequent annealing (SLN+AN) on the tribological behavior of 201J1 austenitic stainless steel. From microstructural observations, the SLN induced grain coarsening and near-surface carbide precipitation. However, the SLN+AN fully formed a highly hardened surface layer (~25 μm thick, 587.2 HV) over a ductile austenite matrix. This hardness gradually decreased toward the core material, indicating a clear hardness gradient.

At the lower load of 10 N, no significant wear loss was observed. However, at an intermediate load of 30 N, the wear mass losses of all specimens increased but still remained comparable, although notable differences in wear depth were observed. This behavior is attributed to the high ductility of the austenite microstructure in the AR and SLN specimens, which promoted plastic deformation and material pile-up at the wear track edges, whereas the SLN+AN specimen maintained a stable, shallow wear track. However, at a high load of 50 N, the SLN+AN specimen transitioned to severe wear with the highest mass loss (2.6 mg) and a drastic increase in wear depth. This occurred because the hard, brittle surface layer fractured under severe stress, whereas the ductile AR and SLN specimens resisted brittle failure and exhibited clear plastic deformation. Furthermore, SEM observations confirmed that the predominant wear mechanism across all specimens was two-body abrasive wear, as evidenced by distinct parallel grooves aligned with the sliding direction.

Both SLN and SLN+AN treatments increased surface roughness compared to the AR condition, indicating that the surface treatments significantly altered the surface morphology. This increased roughness was a primary factor in determining the frictional response, leading the SLN and SLN+AN specimens to generally exhibit higher COF at low load. However, for the surface-treated specimens, the COF decreased with increasing applied load due to surface strain hardening beneath the wear track. Nanoindentation measurements demonstrated that tribological sliding induced significant surface strain hardening in the austenite matrix through dislocation accumulation, mechanical twinning or strain-induced martensitic transformation, particularly at higher loads. While this transformation reduced the COF, the high hardness and brittleness of the martensitic phase did not improve wear resistance. Instead, it led to a brittle fracture, ultimately accelerating material loss. This phenomenon was especially evident in the SLN+AN specimen when compared with the more ductile AR and SLN specimens.

Overall, the SLN+AN treatment is highly effective at improving surface hardness and wear resistance under low to moderate sliding loads. However, its performance significantly deteriorates under high-load conditions due to the brittle failure of the surface-modified layer. These findings highlight the critical need to balance hardness and ductility when designing surface modifications for austenitic stainless steels intended for severe tribological applications, demonstrating that high surface hardness alone is insufficient to ensure good wear resistance under severe loading conditions.

Acknowledgment

The authors would like to express their sincere gratitude to Thai Tohken Thermo CO., LTD. for providing the test specimens and supporting the heat treatment processes. We are also grateful to Ms. Kanokwan Saengkiettiyut and Mr. Nattapol Pintitraratibodee from the Metallurgy and Materials Science Research Institute (MMRI) for their valuable technical assistance, and to the Scientific and Technological Research Equipment Centre (STREC) for the support of analytical equipment. Finally, we would like to thank the Department of Metallurgical Engineering, Faculty of Engineering, Chulalongkorn University, for providing the laboratory space and overall research support.

References

[1] G. Lothongkum, *Stainless steels*. Bangkok: Chulalongkorn press, 2021.

[2] A. Pramanik and A. K. Basak, *Stainless Steel: Microstructure, Mechanical Properties and Methods of Application*. Nova Publisher's, 2015.

[3] M. V. Boniardi and A. Casaroli, *Stainless Steels*. Lucefin S.p.A., 2014.

[4] H. S. Khatak, and B. Raj, *Corrosion of austenitic stainless steels: mechanism, mitigation and monitoring*. Woodhead Publishing, 2002.

[5] M. G. Fontana, *Corrosion Engineering*. Tata McGraw-Hill, 2005.

[6] Y. Katada, K. Hirose, and M. Kumagai, *Nickel-saving Type High Nitrogen Austenitic Stainless Steel*. Springer Japan, 2022.

[7] P. Pistorius, and M. Du Toit, "Low-nickel austenitic stainless steels: Metallurgical constraints," *Proceedings of the 12th International Ferroalloys Congress: Sustainable Future,* pp. 911–917, 2010.

[8] H. Berns, V. Gavriljuk, and S. Riedner, *High Interstitial Stainless Austenitic Steels*. Springer Berlin Heidelberg, 2012.

[9] G. Stachowiak, and A. W. Batchelor, *Engineering Tribology*. Elsevier Science, 2013.

[10] I. Hutchings, and P. Shipway, *Tribology: Friction and wear of engineering materials: Second Edition*. Butterworth-Heinemann, pp. 1-388, 2017.

[11] J. P. Davim, Ed., *Tribology for Engineers: A Practical Guide*. Elsevier Science, 2016.

[12] L. Patnaik, S. Ranjan Maity, and S. Kumar, "Status of nickel free stainless steel in biomedical field: A review of last 10 years and what else can be done," *Materials Today: Proceedings,* vol. 26, pp. 638–643, 2020.

[13] D. Pye, *Practical Nitriding and Ferritic Nitrocarburizing*. ASM International, 2003.

[14] H. S. Luo, and C. Zhao, "Low temperature salt bath hardening of AISI 201 austenitic stainless steel," *Physics Procedia,* vol. 50, pp. 38-42, 2013.

[15] X. Wang, Z. Liu, Y. Chen, J. Sun, Q. He, Q. Liu, G. Liu, and K. Xie, "Abrasive resistance and corrosion properties of AISI 316 sieve via low-temperature gaseous nitriding," *Surface and Coatings Technology,* vol. 361, pp. 349–356, 2019.

[16] ASTM International, *Standard Test Method for Linearly Reciprocating Ball-on-flat Sliding Wear: ASTM G*133-05 (*Reapproved* 2010). ASTM International, 2010.

[17] C. X. Li, and T. Bell, "Sliding wear properties of active screen plasma nitrided 316 austenitic stainless steel," *Wear,* vol. 256, no. 11, pp. 1144–1152, 2004.

[18] P. Visuttipitukul, C. Paa-rai, and K. Hideyuki, "Effect of decarburization on microstructure of DC-plasma nitrided H 13 tool steel," *Journal of Metals, Materials and Minerals,* vol. 16, no. 2, pp. 1–6, 2006.

[19] A. P. Murali, M. Alphonse, D. Ganesan, S. Salunkhe, and H. M. A. M. Hussein, "Sliding wear behaviour of salt bath nitrided 316LN austenitic stainless steel," *Applied Surface Science Advances,* vol. 15, p. 100401, 2023.

[20] M. A. J. Somers, and T. L. Christiansen, "Nitriding of Steels," in *Encyclopedia of Materials: Metals and Alloys*, F. G. Caballero Ed. Oxford: Elsevier, pp. 173–189, 2022.

[21] Y.-S. Kim, S.-D. Kim, and S.-J. Kim, "Effect of phase transformation on wear of high-nitrogen austenitic 18Cr-18Mn-2Mo-0.9N steel," *Materials Science and Engineering: A,* vol. 449–451, pp. 1075-1078, 2007.

[22] A. F. Yetim, and M. Yazıcı, "Wear resistance and non-magnetic layer formation on 316L implant material with plasma nitriding," *Journal of Bionic Engineering,* vol. 11, no. 4, pp. 620–629, 2014.

[23] E. de Araújo Junior, R. M. Bandeira, M. D. Manfrinato, J. A. Moreto, R. Borges, S. dos Santos Vales, P. A. Suzuki, and L. S. Rossino, "Effect of ionic plasma nitriding process on the corrosion and micro-abrasive wear behavior of AISI 316L austenitic and AISI 470 super-ferritic stainless steels," *Journal of Materials Research and Technology,* vol. 8, no. 2, pp. 2180–2191, 2019.

[24] S. K. Singh, C. Naveen, Y. Venkat Sai, U. Satish, C. Bandhavi, and R. Subbiah, "Experimental study on wear resistance of AISI 347 treated with salt bath nitriding and gas nitriding processes -A review," *Materials Today: Proceedings,* vol. 18, pp. 2717–2722, 2019.

[25] N. F. L. Dias, J. Urbanczyk, D. Stangier, P. Köhnen, C. Schaak, S. Höges, and W. Tillmann, "Plasma nitriding of additively manufactured 316L austenitic stainless steel produced by laser power bed fusion and metal binder jetting," *Journal of Materials Research and Technology,* vol. 41, pp. 4056–4066, 2026.

[26] K. Chawla, "Investigation of tribological behavior of stainless steel 304 and grey cast iron rotating against EN32 steel using pin on disc apparatus," *IOSR Journal of Mechanical and Civil Engineering,* vol. 9, pp. 18–22, 2013.

[27] V. Kumar, K. U. Nagegowda, S. B. Boppana, R. Sengottuvelu, and P. Kayaroganam, "Wear behavior of aluminium 6061 alloy reinforced with coated/uncoated multiwalled carbon nanotube and graphene," *Journal of Metals, Materials and Minerals,* vol. 31, no. 1, pp. 17–24, 2021.

[28] C. Lertlummeechai, and P. Sricharoenchai, "Tribological behavior of austenitic stainless steel and vanadium carbide coated by TRD process," *Journal of Metals, Materials and Minerals,* vol. 22, no. 1, pp. 7–12, 2012.

[29] S. Mohanty, and A. K.Senapati, "Study on wear behavior of low nickel austenitic stainless steel by using ball on disc," *Materials Today: Proceedings,* vol. 66, pp. 1961–1967, 2022.

[30] G. Fargas, J. J. Roa, and A. Mateo, "Influence of pre-existing martensite on the wear resistance of metastable austenitic stainless steels," *Wear,* vol. 364-365, pp. 40–47, 2016.

[31] Q. Luo, O. Oluwafemi, M. Kitchen, and S. Yang, "Tribological properties and wear mechanisms of DC pulse plasma nitrided austenitic stainless steel in dry reciprocating sliding tests," *Wear,* vol. 376–377, pp. 1640–1651, 2017.

[32] K. R. Sree, G. K. Reddy, G. L. Prasanna, J. Saranya, A. A. Lakshmi, M. Swetha, T. V. Raj, R. Subbiah, "Dry sliding wear behavior of treated AISI 304 stainless steel by gas nitriding processes," *Materials Today: Proceedings,* vol. 44, pp. 1406–1411, 2021.

[33] X. Yan, J. Hu, X. Zhang, and W. Xu, "Macroscopic and nanoscale investigation of the enhanced wear properties of medium-Mn steel processed via room-temperature quenching and partitioning," *Wear,* vol. 522, p. 204711, 2023.

[34] F. De Barbieri, N. Araya, D. Castro, C. Aguilar, D. Jorge-Badiola, and I. Moran, "Effect of chromium on sliding wear behavior and strain hardening behavior of $Fe_{22}Mn_{0.6}C_{-x}Cr$ TWIP steel," *Journal of Materials Research and Technology,* vol. 36, pp. 6088–6098, 2025.

[35] W. Hübner, "Phase transformations in austenitic stainless steels during low temperature tribological stressing," *Tribology International,* vol. 34, no. 4, pp. 231–236, 2001.

[36] C. Cai, R. Song, S. Liu, Y. Feng, and Z. Pei, "Wear behavior and subsurface layer work hardening mechanism of $Fe_{-24.1}Mn_{-1.21}C_{-0.48}$ Si steel," *Procedia Engineering,* vol. 207, pp. 2251–2256, 2017.

[37] B. Wang, C. Hong, G. Winther, T. L. Christiansen, and M. A. J. Somers, "Deformation mechanisms in meta-stable and nitrogen-stabilized austenitic stainless steel during severe surface deformation," *Materialia,* vol. 12, p. 100751, 2020.